Research Article Vol. 6, No. 7 / July 2019 / Optica 872

Femtosecond phase control in high-field terahertz-driven ultrafast electron sources

Dongfang Zhang,[1,*] Arya Fallahi,[1] Michael Hemmer,[1] Hong Ye,[1] Moein Fakhari,[1,2] Yi Hua,[1] Huseyin Cankaya,[1,2] Anne-Laure Calendron,[1,2] Luis E. Zapata,[1] Nicholas H. Matlis,[1] and Franz X. Kärtner[1,2]

[1]Center for Free-Electron Laser Science, Deutsches Elektronen Synchrotron, Notkestrasse 85, 22607 Hamburg, Germany
[2]Department of Physics and The Hamburg Centre for Ultrafast Imaging, University of Hamburg, Luruper Chaussee 149, 22761 Hamburg, Germany
*Corresponding author: dongfang.zhang@cfel.de

Received 21 March 2019; revised 16 May 2019; accepted 1 June 2019 (Doc. ID 362794); published 11 July 2019

Terahertz-based electron acceleration has recently emerged as a promising candidate for driving next-generation high-brightness electron sources. Although initial demonstrations have proven the feasibility of this technology for accelerating and manipulating the phase space of electrons, further demonstrations of exquisite timing control are required to make use of terahertz acceleration for demanding applications such as light sources and ultrafast electron diffraction. In this paper, we use a two-stage segmented-terahertz-electron-accelerator-and-manipulator (STEAM) setup to demonstrate control over the electron beam energy, energy spread, and emittance. The first rebunching stage is used to tune the duration of 55 keV electron bunches from a DC electron gun that enables femtosecond phase control at the second accelerating stage. For optimized parameters, energy spread and emittance are reduced by 4× and 6×, respectively, relative to operation with the first stage off. A record energy gain of ∼70 keV was achieved at a peak accelerating field of 200 MV/m, resulting in a >100% energy boost in a terahertz-powered accelerator for the first time. These results represent a critical step forward for the practical implementation of terahertz-powered devices in ultrafast electron sources. © 2019 Optical Society of America under the terms of the OSA Open Access Publishing Agreement

https://doi.org/10.1364/OPTICA.6.000872

1. INTRODUCTION

Particle accelerators and ultrafast electron sources have become an essential technology in our society. Many have been brought into daily use in areas as diverse as medical imaging and therapy [1,2], semiconductor device processing [3], and fundamental sciences from physics to structural biology [4–6]. Despite tremendous advances over decades of development, conventional RF-powered devices remain costly, require major infrastructure, and consume significant power, limiting the availability of these technologies to an even broader scientific community [7]. In particular for ultrafast science applications, difficulties in synchronization [8] and low acceleration gradients [9] represent serious challenges for reaching desired spatial and temporal resolutions. Strong motivation thus exists for exploring alternative "compact" technologies offering smaller sizes and costs and the potential to push the resolution frontiers. Applications requiring lower levels of charge (e.g., in the subpicocoulomb range) are especially well suited to this approach.

Terahertz-driven electron acceleration has recently emerged [10–18] as a promising approach for developing compact accelerators. Scaling accelerators to terahertz frequencies offers many advantages: first, the short wavelengths and short pulse durations of the terahertz radiation are expected to enable order-of-magnitude increases in field-induced breakdown thresholds, allowing for greater acceleration gradients; second, existence of efficient, optically based methods for high-field terahertz generation allow intrinsic synchronization among the electrons, the driving fields, and any probe lasers; and third, the millimeter scale of the wavelength, together with the higher field strengths, allows devices to shrink significantly in cost, size, and infrastructure while still being fabricable using conventional means. The millimeter scale of terahertz-based accelerators offers an unexplored compromise between the meter scale of existing RF devices and the micron scale of other laser-based compact accelerator technologies. Examples of these other technologies include dielectric laser accelerators (DLAs) [19,20], which suffer from low charge capacities and extreme fabrication tolerances, and laser-plasma accelerators [21–23], which currently suffer from instabilities and low repetition rates. The picosecond time-scale of the terahertz field variations offer increases in timing precision over RF while still supporting a moderate charge at the picocoulomb level. The terahertz-based electron source has the potential to produce high-repetition, high-energy ultrafast electron bunches, which are highly desired in ultrafast electron diffraction [5,6].

The emergence of terahertz-based accelerators is being supported by the recent growth of ultrafast terahertz sources with electric-field strengths reaching GV/m [24–29]. Proof-of-principle demonstrations [10,13,16,17] with these sources have

resulted in multikilo-electron-volt acceleration, as well as manipulations of electron bunch phase space [16,30,31], proving the feasibility of terahertz-based accelerator technology. However, these initial demonstrations have only started to explore the essential capabilities of this technology and thus leave room for further improvement of basic beam parameters as well as development of terahertz-based methods to control them. Key steps along this development plan include increasing terahertz pulse energies to enable electron energies in the mega-electron-volt range, tuning of the injected electron bunch length, and control over energy spread and emittance [10,16,17].

When bunch acceleration is pursued using fast varying terahertz fields, the bunch length needs to be much shorter than the duration of a terahertz half-cycle. The output of a DC or an RF accelerator except in the ultrarelativistic regime may not provide the required bunch length for terahertz acceleration with minimum energy spread. Therefore, bunch compression schemes need to be implemented in conjunction with terahertz accelerators for optimal performance. In this paper, we exploit the multiple functionalities of the segmented-terahertz-electron-accelerator-and-manipulator (STEAM) device [16] to provide both compression and high-field terahertz-driven acceleration in a staged geometry. The compression is used to reduce the bunch length to subpicosecond duration, thereby providing femtosecond control over the accelerating phase. In this way, the effects of the bunch duration on the terahertz acceleration process are explored. We achieve a peak acceleration field of 200 MV/m, resulting in a record >70 keV terahertz acceleration from an injected 55 keV electron beam resulting in up to ∼125 keV accelerated electrons. By tuning the compression of the injected bunch, femtosecond control over the accelerating phase is achieved, which enables great improvement of both the energy spread and emittance of the electron beam relative to the uncompressed case and compared to previous terahertz-based acceleration demonstrations. These results pave the way for further, highly needed development of this promising technology for practical implementation in applications from high-energy physics to ultrafast-electron diffraction and tabletop radiation sources.

2. CONCEPT AND IMPLEMENTATION

Figure 1(a) shows the schematic view of the experimental setup along with photographs of the actual STEAM-buncher (bunch compressor) and STEAM-linac (linear accelerator), showing their compact size. 55 keV electron bunches are generated from a phototriggered DC gun and injected into a terahertz-powered buncher before injection into a terahertz-powered linac. Both devices derive their terahertz pulses from a single near-infrared (NIR) laser that also triggers the photocathode of the DC gun, resulting in inherent synchronization between the electrons and the accelerating fields. Ultraviolet pulses for photoemission on the photocathode are generated via two consecutive stages of second harmonic generation (SHG) of the fundamental NIR wavelength, which converts the 1020 nm laser first to 510 nm and then to 255 nm. The rest of the NIR laser beam is split into four beams, which are used for generating four single-cycle terahertz pulses via intrapulse difference frequency generation. Two terahertz pulses are then coupled into each STEAM device from the sides (Fig. 1) through symmetric horn structures that guide the terahertz energy to the interaction region transversely relative to the propagation direction of the electrons. Upon entering the interaction region of

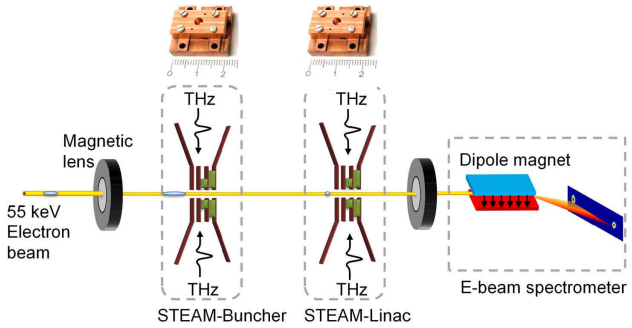

Fig. 1. Schematic illustration of the experimental setup. 55 keV electron bunches are generated by a DC electron gun. The UV pulses are produced from a part of the Yb:YLF laser pulses by two SHG stages and directed onto a gold photocathode generating photoelectrons, which are further accelerated to 55 keV by the DC electric field between the photocathode and anode plate. This Yb:YLF laser also drives four synchronized optical-rectification stages, each generating single-cycle terahertz pulses. The STEAM-buncher is driven by two counterpropagating terahertz beams with energy $\sim 2 \times 50$ nJ for electron compression. The STEAM-linac is driven by $\sim 2 \times 15$ μJ terahertz radiation for electron acceleration.

each STEAM device, the electrons—when correctly timed with the terahertz fields—are subjected to the electric and magnetic components of the Lorentz force: the electric field is responsible for acceleration and deceleration, while the magnetic field induces transverse deflections. Inside the STEAM device, the terahertz beams are split transversely by thin metal sheets into several layers of varying thickness [Figs. 2(a) and 2(b)], each of which acts as a waveguide carrying a fraction of the total energy to the interaction region. Dielectric slabs with tailored lengths are inserted into each layer to match the arrival time of the terahertz wavefront with that of the electrons, thereby quasi-phase-matching the electron-terahertz interaction.

Both of the STEAM devices are operated in the "electric" mode [16], in which the fields are timed to produce electric-field superposition and magnetic-field cancellation at the center of the interaction region. The timing of the electron bunch relative to these fields depends on the function of the STEAM device. In the first device, which acts as an electron buncher, the electrons are

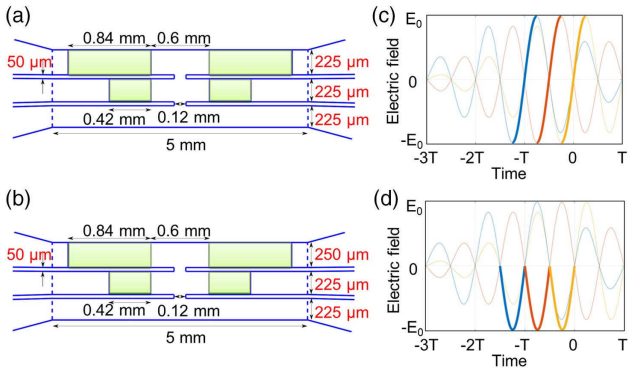

Fig. 2. Design of the segmented waveguide structure. Schematic illustration for (a) buncher and (b) linac. Temporal signature of the electric fields affecting the electron bunch for (c) compression and (d) acceleration. In each layer the electron-terahertz interaction is marked with thick blue, red, and yellow colors.

timed to travel through the zero-crossing of the terahertz field, where the temporal electric-field gradients are maximized and the average field is minimized. This configuration causes acceleration of the electron bunch tail and deceleration of the bunch head, leading to ballistic longitudinal focusing [Figs. 2(a) and 2(c)]. In the second device, which acts as a linac, the electron-terahertz timing is set such that the electron bunch only experiences the negative cycle of the terahertz electric fields, resulting in a net, continuous acceleration [Figs. 2(b) and 2(d)].

The timings of the terahertz and electron beams (and thus the operation mode of each STEAM device) are controlled using motorized delay lines in the corresponding infrared beam lines. The energy spectra of the electron bunches were measured using an electromagnetic dipole oriented to induce vertical deflections onto a microchannel plate (MCP) detector. To determine the electron bunch duration at the acceleration stage, the STEAM device used for the linac was operated in a streaking mode [14] by adjusting the terahertz beam timing so that the electrons experienced uncancelled magnetic fields at their high-gradient zero-crossing point. The NIR drive laser is a cryogenically cooled Yb:YLF system that delivers optical pulses with 1.2 ps duration and 50 mJ energy at 1020 nm wavelength at 10 Hz repetition rate [32,33]. Terahertz pulses with a center frequency of 0.29 terahertz (3.44 ps period) are generated using the tilted pulse-front (TPF) method [24]. Only 2×50 nJ of terahertz energy were used to power the buncher while up to 2×15 μJ were used in the linac. For the latter case, the NIR beam is shaped to create an elliptical terahertz beam [34] so that higher pump energy can be used with reduced depletion effects. The buncher is designed [Fig. 2(a)] with three layers of equal height, $h = \{0.225, 0.225, 0.225\}$ mm, and are fitted with fused silica ($\epsilon_r = 4.41$) slabs of length $L = \{\text{none}, 0.42, 0.84\}$ mm for timing control. The equal heights reflect the fact that no acceleration, and thus no velocity change, occurs [Fig. 2(c)]. The linac [Fig. 2(b)] is designed with three layers of dielectric material of varying height, $h = \{0.225, 0.225, 0.250\}$ mm, optimized for acceleration and fitted with fused silica slabs of length $L = \{\text{none}, 0.42, 0.84\}$ mm. The increasing layer heights of the linac account for the increase in velocity of the subrelativistic electrons during acceleration. Since the energy change in the first and second layers is not very big, the layers were chosen to have the same thickness for easier fabrication. Note, the number of segments in a STEAM device is chosen to achieve a given function, for example compression, with minimum terahertz energy and complexity. For much higher degrees of acceleration, a greater number of layers and a greater degree of height tuning is required to optimize the interaction (see Supplement 1, Fig. S1). The diameter of the entrance and exit apertures of both the buncher and the linac is 120 μm.

The modeling of the experiment accounts for single-cycle Gaussian beams at 0.29 THz center frequency as the output of the laser-driven terahertz source. Equations in Gaussian beam optics are used for the propagation of the terahertz beam in free-space. The evolution of the fields in the coupler, waveguide, and interaction section of the STEAM device are so intricate that considering analytical formulations does not lead to accurate results. Thus, we employ numerical solution of Maxwell equations to model the field propagation inside the STEAM device. For this purpose, an inhouse Maxwell solver based on the discontinuous Galerkin time domain (DGTD) method is developed [35]. The software is written in C++ and is parallelized using the Message Passing Interface (MPI) library. The geometry of the STEAM device is drawn and tessellated using Gmsh software [36] and the Dune library [37] is utilized for mesh and grid management. The metallic boundaries and quartz inclusions of the STEAM device are modeled as a perfect electric conductor and dielectric with permittivity 4.41. Through total-field/scattered-field (TF/SF) boundary conditions, the two Gaussian beams are injected into the computational domain. Using a particle-in cell (PIC) algorithm for solving the equations of motion, electrons are generated and accelerated in the computational model. We expect that such a numerical approach to model the device operation captures all the involved effects and produces reliable simulation results.

3. ACCELERATOR PERFORMANCE

In RF-driven, conventional accelerators, the effects of the temporal extent of the injected electron bunch on the properties of the accelerated bunch are well understood, and are related with the variation in the electric field experienced over the time frame of the interaction by different electrons within the bunch arriving at different times. In general, one can expect larger field gradients and larger bunch durations to lead to larger energy spreads. Injected bunches of larger duration can also lead to higher emittances as they experience a greater fraction of the sinusoidal driving waveform, and hence a larger degree of nonlinearity in the accelerating field. For our terahertz-driven accelerator, the period of the driving field is approximately 200× shorter than for an S-band device, and the supported field strengths are expected to reach approximately 10× higher [9]. The field gradients experienced by electrons in a terahertz-driven accelerator can thus be orders of magnitude higher than those in a conventional device, and the timescale over which the curvature of the field is noticeable is orders of magnitude shorter. The effects of the injected bunch duration are therefore expected to be orders of magnitude more severe. We study these effects in the terahertz regime for the first time by characterizing the performance of our accelerator using injected bunches of varying duration controlled by compression provided by the first STEAM device.

4. ENERGY SPREAD

With the compressor unpowered, 55 keV electron bunches of charge ∼1 fC travelling ∼300 mm from the DC gun to the linac stage were allowed to expand under the influence of space-charge forces to a duration, measured at the linac, of greater than 1000 fs, FWHM [Fig. 4(b)]. At this duration, the electron bunch occupied >60% of the 1.7 ps accelerating field half-wave, leading to a post-acceleration energy spectrum with a peak at 115 keV and a FWHM energy spread of more than 60 keV [Fig. 3(a)]. To compare these results to expectation, we modeled the propagation of electrons, detuned from optimal injection timing, through the linac. These calculations show, as expected, that the electron energy gain is sensitive on a subpicosecond timescale to the injection timing [Fig. 3(b)] which, when optimal, is designed so that an electron experiences a full acceleration half-cycle of the terahertz radiation within each layer [Fig. 3(c)]. Electrons arriving at different times experience less acceleration in the first layer and thus take longer to propagate through it. The detuning is then accentuated in the following layers, resulting in complex dynamics of dephasing and deceleration, and thus a highly nonlinear dependence of the acceleration on timing [Fig. 3(d)]. The variation in

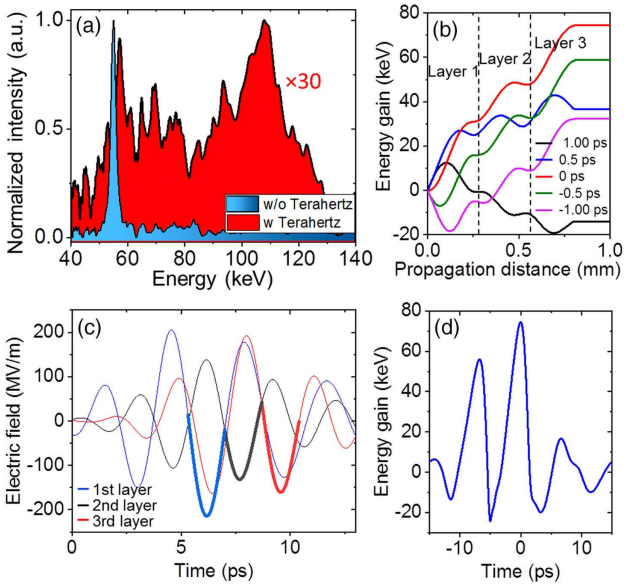

Fig. 3. Acceleration performance. (a) Measured electron energy spectra for input electron beam (blue-shaded curve) and accelerated electron beam (red-shaded curve) with maximum terahertz energy with the buncher turned off. The energy distribution is normalized to the 55 keV input electron beam with around 1 fC bunch charge. An increased energy spread is observed due to the long length of the injected electron bunch and the slippage between the terahertz pulse and the electron bunch. (b) Calculated energy gain along the electron propagation direction for different electron injection times. (c) Accelerating field in the middle of each layer versus time for the designed acceleration condition. The interaction is marked with thick blue, black, and red colors for each layer. (d) Simulated energy gain as a function of the electron injection time. Simulation is performed based on 2 × 15 μJ terahertz energy.

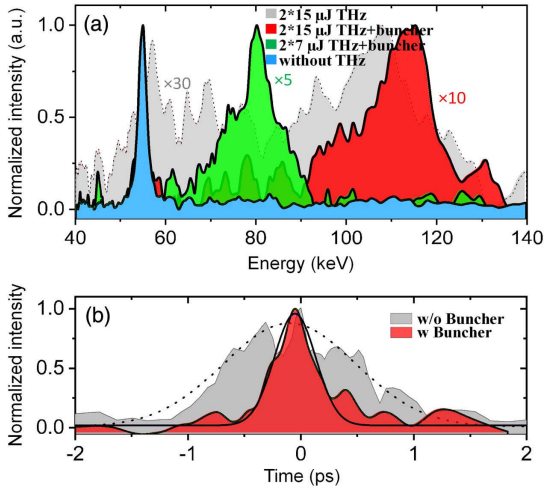

Fig. 4. Energy spread compensation. (a) Measured electron energy spectra for input beam (blue-shaded curve), accelerated beam without buncher (gray-shaded curve) and with buncher (2 × 7 μJ terahertz—green-shaded curve and 2 × 15 μJ terahertz—red-shaded curve). The energy distribution is normalized to the 55 keV input electron beam with around 1 fC bunch charge. (b) Measured input electron pulse duration with (red-shaded curve) and without buncher (gray-shaded curve).

energy gain predicted for electrons injected over a range of ±1 ps, corresponding to the measured input bunch duration, agrees well with the observed energy spread. As can be seen in Fig. 3(a), some injected electrons experience little, or even negative acceleration, consistent with the trajectories shown in Fig. 3(b).

To minimize the negative effects of the bunch temporal extent, the first STEAM device ("buncher," implemented 80 mm downstream of the photocathode and 200 mm upstream of the linac), was operated in a compression mode. The duration of the electron bunch at the linac was optimized to a minimum of ∼350 fs (FHWM) by tuning the terahertz energy applied to the buncher and switching the linac to a streaking mode [16] [Fig. 4(b)]. The minimum bunch duration was set by the duration of the UV photocathode pulse, which was ∼600 fs in duration, and by the distance between the buncher and streaker, which limited the strength of the velocity bunching. This enables femtosecond precision of injection phase in the accelerating stage. Figure 4(a) shows that the energy spread of the compressed electron bunch after the optimized acceleration in the linac is reduced by a factor of ∼4 as compared to the uncompressed case. As a result, unlike the uncompressed case, the energy spectrum is cleanly shifted in its entirety to higher energies by the acceleration. The peak of the accelerated energy spectrum is about 115 keV, and the high-energy tail reaches about 125 keV. These results represent a new record terahertz-driven acceleration of 70 keV, and a corresponding peak field of 200 MV/m, which was estimated using the simulation results shown in Figs. 3(b) and 3(c), based on 2 × 15 μJ of coupled terahertz pulse energy. The asymmetry of the energy spectrum [Fig. 5(b)] about the peak is because the bunch center is accelerated most while both the bunch head and tail are accelerated less [38]. As described above, the energy spread is affected not only by the bunch duration but also by the field gradient. Figure 4(a) shows that, as expected, the absolute

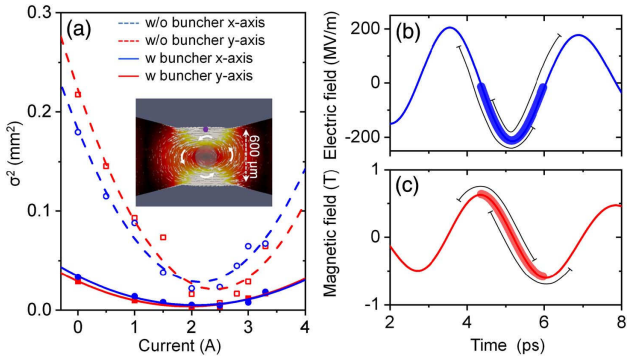

Fig. 5. Emittance measurement. (a) Measured root-mean-square beam size (σ) as a function of solenoid current for the uncompressed (hollow markers) and compressed (solid markers) electron bunches in the x-horizontal (red squares) and y-vertical (blue dots) directions. The transverse emittance was determined using parabolic fits to the data. For the uncompressed bunch the fits (dashed lines) yielded emittances of $\varepsilon_{x,n} =$ 1.703 mm mrad and $\varepsilon_{y,n} =$ 1.491 mm mrad for horizontal and vertical directions, respectively, and similarly for the compressed bunch, the fits (solid lines) yielded $\varepsilon_{x,n} =$ 0.285 mm mrad and $\varepsilon_{y,n} =$ 0.246 mm mrad, respectively. (Inset) Snapshot of the simulated magnetic field distribution in the first layer of the STEAM device. (b) Electric field of the first layer as a function of time. The thick blue line represents the optimized interaction window, and the black lines are detuned ones. (c) Magnetic field of the first layer as a function of time at the top middle part marked by the magenta dot in the (a) inset. The thick red line represents the optimized interaction window, and the black lines are detuned windows.

energy spread of the accelerated electron bunches is indeed correlated to the amount of acceleration, which was controlled by varying the applied terahertz energy and thus the applied field strength. An even shorter bunch length is desired to further decrease the energy spread.

5. EMITTANCE

The transverse emittance is determined by scanning the current of a focusing solenoid and measuring the size of the electron beam profile on the MCP [39]. In the case of an uncompressed injection beam, parabolic fits to beam size versus current reveal a transverse emittance in the horizontal and vertical directions of $\varepsilon_{x,n} = 1.703$ mm mrad and $\varepsilon_{y,n} = 1.491$ mm mrad, respectively [Fig. 5(a)]. Implementing compression of the injected electron bunch improved the measured transverse emittance by a factor of 6, to $\varepsilon_{x,n} = 0.285$ mm mrad and $\varepsilon_{y,n} = 0.246$ mm mrad, respectively. Note that the emittance reduction factor is roughly twice that for the reduction of bunch duration, which is a measure for the nonlinearity of the interaction dynamics with time where the electrons experience strong focusing and defocusing magnetic field during acceleration [Figs. 5(b) and 5(c)]. The emittance reduction is due in part to the reduction in energy spread, caused by the reduction in the range of accelerating and decelerating forces experienced as well as to a reduction in the transverse momentum spread, caused by the reduction in the range of focusing and defocusing fields experienced [14]. As can be seen in Fig. 5(b), electrons injected at the optimal timing experience the entire accelerating half-cycle of the E-fields, while electrons arriving before or after optimal timing experience less of the accelerating half-cycle and also some of the decelerating half-cycle. The result is that electrons timed before or after the optimum both see less energy gain.

A similar effect occurs with the B-field interaction. Although on axis, i.e., along the center line of the interaction zone, the magnetic field is, in principle, perfectly canceled, at spatial points off axis; the B-field is not cancelled and has a pattern of field vectors that circulates around the axis [Fig. 5(a) inset]. Electrons injected at the optimum timing experience a symmetric amount of positive and negative magnetic fields, integrated over the interaction within a given layer. In other words, the temporal window of the interaction covers a half-cycle of the magnetic field from the crest to the trough. In this case, the net deflection of the electron by the B-field is zero. Detuning the injection to earlier times, however, shifts the temporal window so that it includes more of the positive field and less of the negative one, or vice versa for later times [Fig. 5(c)]. As a result, an electron experiences a net deflection to the left, right, up, or down, depending on its position relative to the axis, resulting in an increase in transverse momentum corresponding to a focusing or defocusing of the beam. As this effect is not linear with temporal detuning, the emittance of the bunch grows with the bunch duration.

It is therefore clear that the performance of the accelerator will improve as the duration of the bunch decreases when the space charge effect is negligible. In the work described here, the achievable bunch duration was limited by the experimental geometry; however, in principle, reaching bunch durations significantly below 100 fs is feasible and would greatly improve the quality of the beam. Other schemes to improve beam quality include reducing the layer heights and increasing the number of them so that the fraction of the fields experienced by the electrons in each layer is less than a half-cycle. This strategy, however, introduces higher demands on the fabrication process and potentially increases the impact of fringing fields at the holes between adjacent layers. Further exploration is thus required.

6. CONCLUSION

We present measurements quantifying the effects of detuning the injection timing in a terahertz-powered accelerator on the emittance and energy spread of the accelerated beam. Femtosecond control over the injection-time detuning was achieved by adjusting the duration of the injected electron bunch with a terahertz-powered compression stage. A threefold compression from 1 to 0.35 ps resulted in a 4× improvement in energy spread and a 6× improvement in transverse emittance. These measurements represent a first step in characterizing the operation space and parameter sensitivity of terahertz-driven accelerators. We also demonstrate a new record in a terahertz-driven electron energy gain of ∼70 keV corresponding to a peak accelerating field of ∼200 MV/m using ∼30 μJ of single-cycle terahertz energy. These demonstrations represent a high degree of control over the acceleration process compared to other compact acceleration technologies currently being investigated. This work represents a critical step forward in the development of this technology by transitioning from a proof-of-principle mode of research to a process of development in which the performance and limitations of the new technology can be studied. Our results agree well with both simulations and analytical estimates and thus provide encouraging evidence for increased performance when scaling to sub-100 fs injection bunches and millijoule-scale terahertz pulses reaching GV/m fields, both of which are feasible today. Terahertz-driven acceleration is thus showing itself to be increasingly promising as a realistic alternative as compact, relativistic electron sources for future ultrafast electron diffraction and free-electron lasers.

Funding. Seventh Framework Programme (FP7) FP7/2007-2013 European Research Council (ERC) (609920); Deutsche Forschungsgemeinschaft (DFG) (DFG-EXC1074, SPP1840 SOLSTICE); Gordon and Betty Moore Foundation (GBMF4744).

Acknowledgment. We gratefully acknowledge T. Tilp and M. Schust for the expert technical support and for the fabrication of the accelerator devices used in this work. We would like to acknowledge manufacturing of the magnetic steer for energy measurement by the group of Dr. Ralph Aßmann at DESY. The authors also thank T. Y. Fan and J. Zayhowski from MIT Lincoln Laboratory for initial work on the cryogenic Yb:YLF laser within the AXIS Program funded by the Defense Advanced Research Projects Agency (DARPA) and DARPA for the loan of the laser. A.-L.C acknowledges support through a Helmholtz Postdoctoral Fellowship from the Helmholtz Association.

See Supplement 1 for supporting content.

REFERENCES

1. U. Amaldi, "Cancer therapy with particle accelerators," Nucl. Phys. A **654**, C375–C399 (1999).
2. M. Durante and J. S. Loeffler, "Charged particles in radiation oncology," Nat. Rev. Clin. Oncol. **7**, 37–43 (2010).

3. R. W. Hamm and M. E. Hamm, *Industrial Accelerators and Their Applications* (World Scientific, 2012).
4. J. C. H. Spence and H. N. Chapman, "The birth of a new field," Philos. Trans. R. Soc. B **369**, 20130309 (2014).
5. J. Yang, X. Zhu, T. J. A. Wolf, Z. Li, J. P. F. Nunes, R. Coffee, J. P. Cryan, M. Gühr, K. Hegazy, T. F. Heinz, K. Jobe, R. Li, X. Shen, T. Veccione, S. Weathersby, K. J. Wilkin, C. Yoneda, Q. Zheng, T. J. Martinez, M. Centurion, and X. Wang, "Imaging CF 3 I conical intersection and photodissociation dynamics with ultrafast electron diffraction," Science **361**, 64–67 (2018).
6. T. Ishikawa, S. A. Hayes, S. Keskin, G. Corthey, M. Hada, K. Pichugin, A. Marx, J. Hirscht, K. Shionuma, K. Onda, Y. Okimoto, S.-Y. Koshihara, T. Yamamoto, H. Cui, M. Nomura, Y. Oshima, M. Abdel-Jawad, R. Kato, and R. J. D. Miller, "Direct observation of collective modes coupled to molecular orbital-driven charge transfer," Science **350**, 1501–1505 (2015).
7. S. Manz, A. Casandruc, D. Zhang, Y. Zhong, R. A. Loch, A. Marx, T. Hasegawa, L. C. Liu, S. Bayesteh, H. Delsim-Hashemi, M. Hoffmann, M. Felber, M. Hachmann, F. Mayet, J. Hirscht, S. Keskin, M. Hada, S. W. Epp, K. Flöttmann, and R. J. D. Miller, "Mapping atomic motions with ultrabright electrons: towards fundamental limits in space-time resolution," Faraday Discuss. **177**, 467–491 (2015).
8. H. Yang, B. Han, J. Shin, D. Hou, H. Chung, I. H. Baek, Y. U. Jeong, and J. Kim, "10-fs-level synchronization of photocathode laser with RF-oscillator for ultrafast electron and X-ray sources," Sci. Rep. **7**, 39966 (2017).
9. M. Dal Forno, V. Dolgashev, G. Bowden, C. Clarke, M. Hogan, D. McCormick, A. Novokhatski, B. Spataro, S. Weathersby, and S. G. Tantawi, "Experimental measurements of RF breakdowns and deflecting gradients in mm-wave metallic accelerating structures," Phys. Rev. Accel. Beams **19**, 051302 (2016).
10. E. A. Nanni, W. R. Huang, K.-H. Hong, K. Ravi, A. Fallahi, G. Moriena, R. J. Dwayne Miller, and F. X. Kärtner, "Terahertz-driven linear electron acceleration," Nat. Commun. **6**, 8486 (2015).
11. A. Fallahi, M. Fakhari, A. Yahaghi, M. Arrieta, and F. X. Kärtner, "Short electron bunch generation using single-cycle ultrafast electron guns," Phys. Rev. Accel. Beams **19**, 081302 (2016).
12. W. Ronny Huang, A. Fallahi, X. Wu, H. Cankaya, A.-L. Calendron, K. Ravi, D. Zhang, E. A. Nanni, K.-H. Hong, and F. X. Kärtner, "Terahertz-driven, all-optical electron gun," Optica **3**, 1209–1212 (2016).
13. D. A. Walsh, D. S. Lake, E. W. Snedden, M. J. Cliffe, D. M. Graham, and S. P. Jamison, "Demonstration of sub-luminal propagation of single-cycle terahertz pulses for particle acceleration," Nat. Commun. **8**, 421 (2017).
14. W. R. Huang, E. A. Nanni, K. Ravi, K. H. Hong, A. Fallahi, L. J. Wong, P. D. Keathley, L. E. Zapata, and F. X. Kartner, "Toward a terahertz-driven electron gun," Sci. Rep. **5**, 14899 (2015).
15. M. Fakhari, A. Fallahi, and F. X. Kärtner, "THz cavities and injectors for compact electron acceleration using laser-driven THz sources," Phys. Rev. Accel. Beams **20**, 041302 (2017).
16. D. Zhang, A. Fallahi, M. Hemmer, X. Wu, M. Fakhari, Y. Hua, H. Cankaya, A. L. Calendron, L. E. Zapata, N. H. Matlis, and F. X. Kärtner, "Segmented terahertz electron accelerator and manipulator (STEAM)," Nat. Photonics **12**, 336–342 (2018).
17. E. Curry, S. Fabbri, J. Maxson, P. Musumeci, and A. Gover, "Meter-scale terahertz-driven acceleration of a relativistic beam," Phys. Rev. Lett. **120**, 094801 (2018).
18. J. Hebling, J. A. Fülöp, M. I. Mechler, L. Pálfalvi, C. Tőke, and G. Almási, "Optical manipulation of relativistic electron beams using THz pulses," arXiv:1109.6852 (2011), pp. 1–4.
19. E. A. Peralta, K. Soong, R. J. England, E. R. Colby, Z. Wu, B. Montazeri, C. McGuinness, J. McNeur, K. J. Leedle, D. Walz, E. B. Sozer, B. Cowan, B. Schwartz, G. Travish, and R. L. Byer, "Demonstration of electron acceleration in a laser-driven dielectric microstructure," Nature **503**, 91–94 (2013).
20. J. Breuer and P. Hommelhoff, "Laser-based acceleration of nonrelativistic electrons at a dielectric structure," Phys. Rev. Lett. **111**, 134803 (2013).
21. V. Malka, J. Faure, Y. A. Gauduel, E. Lefebvre, A. Rousse, and K. T. Phuoc, "Principles and applications of compact laser-plasma accelerators," Nat. Phys. **4**, 447–453 (2008).
22. W. Leemans and E. Esarey, "Laser-driven plasma-wave electron accelerators," Phys. Today **62**(3), 44–49 (2009).
23. D. Guénot, D. Gustas, A. Vernier, B. Beaurepaire, F. Böhle, M. Bocoum, M. Lozano, A. Jullien, R. Lopez-Martens, A. Lifschitz, and J. Faure, "Relativistic electron beams driven by kHz single-cycle light pulses," Nat. Photonics **11**, 293–296 (2017).
24. J. Hebling, G. Almasi, I. Kozma, and J. Kuhl, "Velocity matching by pulse front tilting for large area THz-pulse generation," Opt. Express **10**, 1161–1166 (2002).
25. S.-W. Huang, E. Granados, W. R. Huang, K.-H. Hong, L. E. Zapata, and F. X. Kärtner, "High conversion efficiency, high energy terahertz pulses by optical rectification in cryogenically cooled lithium niobate," Opt. Lett. **38**, 796–798 (2013).
26. J. A. Fülöp, Z. Ollmann, C. Lombosi, C. Skrobol, S. Klingebiel, L. Pálfalvi, F. Krausz, S. Karsch, and J. Hebling, "Efficient generation of THz pulses with 0.4 mJ energy," Opt. Express **22**, 20155–20163 (2014).
27. C. Vicario, M. Jazbinsek, A. V. Ovchinnikov, O. V. Chefonov, S. I. Ashitkov, M. B. Agranat, and C. P. Hauri, "High efficiency THz generation in DSTMS, DAST and OH1 pumped by Cr:forsterite laser," Opt. Express **23**, 4573–4580 (2015).
28. R. Köhler, A. Tredicucci, F. Beltram, H. E. Beere, E. H. Linfield, A. G. Davies, D. A. Ritchie, R. C. Iotti, and F. Rossi, "Terahertz semiconductor-heterostructure laser," Nature **417**, 156–159 (2002).
29. M. Tonouchi, "Cutting-edge terahertz technology," Nat. Photonics **1**, 97–105 (2007).
30. A. Ryabov, W. Schneider, P. Baum, D. Ehberger, C. Kealhofer, and F. Krausz, "All-optical control and metrology of electron pulses," Science **352**, 429–433 (2016).
31. J. Fabiańska, G. Kassier, and T. Feurer, "Split ring resonator based THz-driven electron streak camera featuring femtosecond resolution," Sci. Rep. **4**, 5645 (2014).
32. M. Hemmer, L. E. Zapata, Y. Hua, and F. X. Kärtner, "Addressing spectral narrowing in cryogenic Yb:YAG: a 10 mJ cryogenic Yb:YLF regenerative amplifier," in *Lasers Congress (ASSL, LSC, LAC)* (OSA, 2016), paper ATh4A.3.
33. A.-L. Calendron, J. Meier, M. Hemmer, L. E. Zapata, F. Reichert, H. Cankaya, D. N. Schimpf, Y. Hua, G. Chang, A. Kalaydzhyan, A. Fallahi, N. H. Matlis, and F. X. Kärtner, "Laser system design for table-top x-ray light source," High Power Laser Sci. Eng. **6**, e12 (2018).
34. S.-C. Zhong, J. J. Li, Z.-H. Zhai, L.-G. Zhu, J. J. Li, P.-W. Zhou, J.-H. Zhao, and Z.-R. Li, "Generation of 019-mJ THz pulses in LiNbO_3 driven by 800-nm femtosecond laser," Opt. Express **24**, 14828–14835 (2016).
35. A. Fallahi and F. Kärtner, "Field-based DGTD/PIC technique for general and stable simulation of interaction between light and electron bunches," J. Phys. B **47**, 234015 (2014).
36. C. Geuzaine and J. F. Remacle, "Gmsh: A 3-D finite element mesh generator with built-in pre- and post-processing facilities," Int. J. Numer. Methods Eng. **79**, 1309–1331 (2009).
37. M. Blatt, A. Burchardt, A. Dedner, C. Engwer, J. Fahlke, B. Flemisch, C. Gersbacher, C. Gräser, F. Gruber, C. Grüninger, D. Kempf, R. Klöfkorn, T. Malkmus, S. Müthing, M. Nolte, M. Piatkowski, and O. Sander, *The Distributed and Unified Numerics Environment, Version 2.4* (2016), Vol. **4**.
38. J. Shao, C. Jing, S. Antipov, M. Conde, W. Gai, Q. Gao, G. Ha, W. Liu, N. Neveu, J. G. Power, J. Qiu, D. Wang, Y. Wang, E. Wisniewski, L. Zheng, and J. Shi, "Recent two-beam acceleration activities at Argonne wakefield accelerator facility," in *IPAC* (2017), pp. 3305–3307.
39. M. Hachmann and K. Flöttmann, "Measurement of ultra low transverse emittance at REGAE," Nucl. Instrum. Methods Phys. Res. Sect. A **829**, 318–320 (2016).

131.169.55.175 {ts '2019-11-11 04:36:15'}